Annealing environment effects on the electrochemical behavior of supercapacitors using Ni foam current collectors

Annealing Environment Effects on the Electrochemical Behavior of Supercapacitors using Ni Foam Current Collectors

Vijaykumar V. Jadhav[a,b,f], Rohan M. Kore[d], Nanasaheb D. Thorat[e], Je Moon Yun[a], Kwang Ho Kim[a], Rajaram S. Mane[a,c]*, Colm O'Dwyer[b,g,h]*

[a]*School of Materials Science and Engineering, Pusan National University, San 30 Jangjeon-dong, Geumjeong-gu, Busan 609-735, Republic of Korea*
[b]*School of Chemistry, University College of Cork, Cork T12 YN60, Ireland*
[c]*School of Physical Sciences, SRTM, University, Nanded, India*
[d]*Supercapacitive Studies Laboratory, School of Physical Sciences, Solapur University, Solapur, 413255, India*
[e]*Department of Physics, and Bernal Institute, University of Limerick, Limerick, Ireland*
[f]Department of Physics, Shivaji Mahavidyalaya, Udgir, MH, India
[g]*Micro-Nano Systems Centre, Tyndall National Institute, Lee Maltings, Cork T12 R5CP, Ireland*
[h]*Environmental Research Institute, University College Cork, Lee Road, Cork T23 XE10, Ireland*

KEYWORDS: Nickel foam, NiO, annealing, oxidation, electrochemistry, supercapacitor

ABSTRACT

Nickel (Ni) foam-based symmetric/asymmetric electrochemical supercapacitors benefit from a randomly 3D structured porous geometry that functions as an active material support and as a current collector. The surface composition stability and consistency of the current collector is critical for maintaining and consistency supercapacitor response, especially for various mass loading and mass coverage. Here we detail some annealing environment conditions that change the surface morphology, chemistry and electrochemical properties of Ni foam by NiO formation. Air-annealing at 400 and 800 °C and annealing also in N_2 and Ar at 800°C result in the in-situ and ex-situ formation of NiO on the Ni foam (NiO@Ni). Oxidation of Ni to NiO by several mechanisms in air and inert atmospheres to form an NiO coating is subsequently examined in supercapacitors, where the electrochemical conversion through $Ni(OH)_2$ and NiOOH phases influence the charge storage process. In parallel, the grain boundary density reduction by annealing improves the electronic conductivity of the foam current collector. The majority of stored charge occurs at the oxidized Ni-electrolyte interface. The changes to the Ni metal surface that can be caused by chemical environments, heating and high temperatures that typically occur when other active materials are grown on Ni directly, should be considered in the overall response of the electrode, and this may be general for metallic current collectors and foams that can oxidize at elevated temperatures and become electrochemically active.

*Corresponding Authors. *Emails: rajarammane70@srtmun.ac.in (Rajaram S. Mane, Prof.); c.odwyer@ucc.ie (C. O'Dwyer)

1. INTRODUCTION

The ever-growing human population demand on energy resources and the rapid industrial development of portable electronics, electric vehicles and the growing use of renewable and clean energies requires high-performance electrochemical energy conversion and storage devices like fuel cells, batteries and electrochemical supercapacitors (ECs). Of these, ECs (including pseudocapacitors, double layer capacitors, and symmetric and asymmetric capacitors) have attracted intense attention as promising electrochemical energy storage devices due to their fast and efficient energy storage capabilities. They exhibit higher power density and longer lifespan compared to rechargeable lithium-ion batteries, and higher energy density compared with traditional dielectric capacitors [1-2]. Electrochemical double layer capacitor materials are basically carbon based materials like, activated carbon, single/multi-walled carbon nanotubes, graphene etc., which stores charges at electrode/electrolyte interface. On the other hand, in pseudocapacitors or redox supercapacitors charge is stored through fast and reversible surface/near-surface processes and transition metal oxides/hydroxides, carbonates and conducting polymers etc., are some materials of this category [3].

Carbonaceous SCs have limited electrochemical performance (generally measured as specific capacitance) but long lasting cycle life whereas carbonates or conducting polymer-based materials demonstrate low operating potential window and a weaker chemical/environmental stability. However, recently developed symmetric/asymmetric EC devices can achieve reasonably high energy density as well as high power density along with a larger operating cell voltage. Fabrication of such symmetric/asymmetric devices often requires active material combinations such as metal oxide||metal oxide, conducting polymers||conducting polymer, metal oxide||carbon based materials etc., a suitable electrolyte and a current collector (substrate) [4-8]. The current collector is an important constituent of ECs, and often used as the substrates on which further material fabrication is made for electrodes of symmetric/asymmetric supercapacitor devices. Substrates such as graphite [9], gold (layer) on glass [10], aluminum [11], stainless-steel [12], carbon cloth [13], Si-Pt based foils [14], nickel-based metallic foams [15-18] etc., are commonly used in electrochemical energy storage devices as current collectors as well as active mass supporters. It has been proven that the active material nanostructures supported on 3D substrates facilitate larger surface area, easy electrolyte access to the electrode, efficient electron transfer and faster ion transportation, which has allow electrodes them to achieve high contact area for promoting the ion transportation rate, improving the utilization of electrochemically active material [19−24] for optimum performance.

Nickel (Ni) foam-based symmetric/asymmetric electrochemical supercapacitor investigations have recently gained considerable attention due to their 3D structure, high electrical conductivity, low cost and relative abundance [25]. In most of the reported studies, though Ni-foam has been vigorously used as base material, less attention has been paid to its own properties in spite of several decades of knowledge on Ni oxides in strong base. In general, the mass of active material is typically the difference between Ni-foam plus active material and that of Ni-foam itself. This measurement translates to specific capacity and related calculations when used to store charge. Often, the Ni foam is used as the support on which material is grown, in air and relatively high temperatures [14-18], which affect the grain structure on the surface phase of the Ni. Here we report the structure, surface morphology and electrochemical properties of Ni-foam after air-annealing (O_2) at 400 and 800°C temperatures, and compare it to Ni foam annealed in nitrogen (N_2) and Argon (Ar) atmospheres at 800°C and show how they are different to pristine Ni-foam. Due to oxidation of nickel, nickel oxide (NiO), a secondary phase, is developed on Ni-foam whose crystallinity and coverage varies with annealing environments. The study confirms that mass calculations and the nature of the electrochemical response of electrodes using Ni foam should consider the presence of NiO and related phases instead of only two i.e. Ni-foam and active material, which tends to be common practice.

2. EXPERIMENTAL SECTION

Ni-foam (labeled hereafter as Ni) was purchased from Artenano Company limited (Hong Kong) with pore-density of 110 PPI and mass density of 320 gm^2 and was used for the further studies. Pieces of Ni were obtained in ~ 1 × 2 cm^2 dimensions were air-annealed at 400 and 800°C for 1 h in an annealing furnace, labelled as NiO@Ni (400°C) and NiO@Ni (800°C) and also annealed in nitrogen and argon atmospheres at 800 °C, labeled as NiO@Ni (N_2–800°C) and NiO@Ni (Ar–800°C). To observe the effect of annealing at different temperatures in air atmosphere (i.e. 400 and 800°C) and the effect of different annealing atmosphere (at 800°C) on the structural, morphological and electrochemical properties of Ni were measured. The weight of NiO formed on the Ni foam surface was determined by the weight difference method. The average weight increase found onto each sample is ~0.55-0.70 mg. To observe the phase change due to air-annealing, X-ray diffraction patterns (XRD, D8-Discovery Brucker, Cu Kα, 40 kV, 40 mA) of pristine, 400 and 800°C air-annealed Ni and the samples annealed in nitrogen and argon atmosphere at 800°C were obtained in a scanning range of 20-80^o with a 0.02^o step size (2Θ). Raman spectra of NiO@Ni (800°C), NiO@Ni (N_2-800°C) and NiO@Ni (Ar-800°C) were acquired on a Jobin-Yvon Horibra LABRAM-HR800 UV Raman spectrometer with a diode laser of wavelength 514 nm as the excitation source. Field-emission scanning electron microscope (FESEM, Hitachi, S-4800, 15 kV) digital plane-view images were used to examine the surface morphology change. X-ray photoelectron-

spectroscopy (XPS) measurements were carried out using surface analysis system (VG Scientifics ESCALAB250) using a monochromatic Al Kα source (1486.6 eV) to analyze the bonding of Ni-foam and NiO@Ni (800°C) samples. The XPS spectra were calibrated to the carbon C 1s peak at 284.6 eV.

The electrochemical measurements were performed using a three-electrode electrochemical system in 6 mol dm^{-3} KOH electrolyte solution at room temperature (25°C). A platinum plate and SCE were used as the counter and reference electrodes, respectively. Cyclic-voltammetry (CV), galvanostatic charge-discharge (GCD) and electrochemical impedance spectroscopy (EIS) measurements were performed on an Ivium-n-Stat electrochemical workstation (Ivium, Netherlands).

3. RESULTS AND DISCUSSION

Figure 1 (a) shows digital photographs of the Ni, NiO@Ni (400°C) and NiO@Ni (800°C) foam samples where the change in surface appearance, caused by air-annealing, is clearly noticed. Qualitatively, the surface changes from silvery white to black on air-annealing is expected if NiO forms on Ni. Figure 1 (b) shows the XRD patterns obtained from Ni, NiO@Ni (400°C) and NiO@Ni (800°C) samples. The Ni shows three prominent peaks at 44.59°, 51.94° and 76.45° corresponding to the (111), (200) and (220) reflections from cubic Ni (JCPDS-04-0850). However, after annealing at 400 and 800°C for 1 h, the X-ray diffraction patterns undergo changes due to NiO formation. At 800°C air-annealing temperature reflections from crystalline NiO from the (111), (200), (220) and (113) (JCPDS- 47-1049) planes appear at 37.74°, 43.74°, 63.28° and 75.78°, supporting the formation of NiO@Ni. Along with the three prominent reflections from cubic Ni, the XRD patterns of NiO@Ni (N_2-800°C) and NiO@Ni (Ar-800°C) samples consist of the reflections at 37.74°, 43.74°, 63.28° and 75.78° corresponding to the (111), (200), (220) and (113) planes (JCPDS-47-1049), supporting the formation of NiO@Ni as shown in Figure 1 (c).

The plausible mechanism involved in this process of crystallization/recrystallization was also reported elsewhere [26-28]. In the initial stage of air-annealing, the Ni atoms redistribute to preferred sites and interact with the atmosphere oxygen (crystallization). Furthermore, annealing in air initiates nucleation sites for the partial formation NiO (re-crystallization) at lower temperatures and occurs throughout the Ni surface. However, in the latter case for air-annealing above 400 °C, the growth of oxide is dominated by the diffusion of Ni^{+} ions into this NiO layer. Oxygen may penetrate to the surface NiO through the redistributed sites, stimulated by metal diffusion at higher temperature. Also, if the Ni^{+} cations from the NiO@Ni interface diffuse faster than the O^{-} anions, the may reaches the oxygen atoms first and may be responsible for the recrystallization to form NiO@Ni. In other words, oxidation of Ni caused by air-annealing (transfer of electrons through the interface to form a monolayer of adsorbed oxygen ions at the surface) together with the diffusion of oxygen anions into the Ni metal forms NiO whose physicochemical

properties are different than pristine Ni. However, the plausible mechanism involved during the annealing of the nickel foam in nitrogen and argon atmosphere considers ionization of surface Ni. At 800°C, the ionization of nitrogen and argon gas into N^- and Ar^- ions, respectively, may occur. These ionized gas molecules may insert into the Ni lattice sites and loosely bond with the Ni^+ atoms. Due to the weak bonding of N^- and Ar^- ions, the atmospheric O^{2-} ions upon subsequent exposure to air may readily react with Ni^+ atoms and will replace the nitrogen and argon ions and hence the oxidation of Ni foam will form NiO@Ni.

Raman spectra of the NiO@Ni(800°C), NiO@Ni(N_2-800°C) and NiO@Ni(Ar-800°C) samples are shown in Figure 2. It has been observed that the peak observed at 513 cm^{-1} corresponds to longitudinal optical (LO) modes of NiO.[17, 29] Figure 3(a-e) shows the surface morphological analysis of Ni, NiO@Ni (400°C), NiO@Ni (800°C), NiO@Ni (N_2-800°C), and NiO@Ni(Ar-800°C) samples from FE-SEM digital plan-view images. Figure 3 (a) shows the planar surface appearance of Ni samples. Sharp edged grains of irregular dimensions are clear without any treatment, however, as the samples were annealed at 400°C (figure 3(b)) dense and small granular type of morphology was obtained from classical grain boundary size reduction. The re-crystallization of the Ni surface as discussed in the plausible mechanism, is evident whereby partial formation of NiO is found throughout the sample surface. Figure 3(c) shows the FESEM plan view images of NiO@Ni(800°C). The image clearly indicates porous and rough surface is formed with non- homogeneously distributed larger grains. This may be attributed to more efficient Ni^+ diffusion at higher annealing temperature (on smaller grains) resulting in the formation of a thicker NiO layer on the Ni surface as NiO@Ni. [28] A similar mechanism may also be applicable in the cases where the Ni foam was deposited by electro-active material through which the Ni^+ ions become diffused through the material and interact with the oxygen to form NiO during the case of air annealing. Whereas, in the case of Ni foam annealing in different environments such as N_2 and Ar, the crystallization process occurring is through the loose bonding of the N^- and Ar^- ions at 800°C, respectively, which further recrystallizes to NiO by replacing these loosely bonded ions by atmospheric O^{2-} ions when exposed to air upon cooling. This process of crystallization/recrystallization, contributes to the formation of uniformly distributed porous, granular and rough surface morphology of NiO@Ni, as evidenced from Figure 3(d) and Figure 3(e), for N_2 and Ar atmosphere annealing, respectively.

To validate the formation of NiO on the Ni foam surface, XPS analysis was performed on untreated Ni and NiO@Ni (800°C) as shown in Figure 4. As shown in the core-level photoemission spectra of the Ni 2p for both samples, the peaks appearing at 855.8 and 873.8 eV with respective satellite peaks at 861.1 and 878.9 eV, correspond to spin-orbit coupling fine structure of the Ni $2p_{3/2}$ level and the Ni $2p_{1/2}$ levels respectively. [30-32] The O 1s spectrum of both samples has two peaks at 529.7 and 530.7 eV which were

attributed to the O^{2-} in the Ni-O bond.[33] The peak intensity in O 1s spectrum for NiO@Ni(800°C) at 529.7 eV is much larger than that of Ni sample peak. This indicates that the surface of the sample is converted into the NiO. In C 1s spectra, the peak at 284.6 eV is the characteristic photoemission of adventitious carbon.[34]

To investigate the effect of annealing temperature in air as well as the effect of annealing environment on the electrochemical performance of Ni foam, the electrochemical properties of Ni, NiO@Ni(400°C), NiO@Ni(800°C), NiO@Ni(N_2-800°C) and NiO@Ni(Ar-800°C) samples were examined using CV, GCD and EIS measurements in 6 mol dm^{-3} KOH aqueous electrolyte using three electrode cell with SCE and platinum plate as reference and counter electrodes, respectively. Figure 5 (a) shows the CV curves obtained for Ni, NiO@Ni(400°C) and NiO@Ni(800°C) at a scan rate of 10 mV/s within a potential window of 0-0.6 V *vs.* SCE. The CV of Ni indicates a negligible current response. However, for the Ni samples annealed at 400 and 800°C the respective anodic and cathodic sweeps indicate pseudocapacitive behaviour from the annealed Ni foams. The CV curve of the sample NiO@Ni(400°C) composed of redox peak during the cathodic sweep at 0.32 V corresponding to the conversion of surface NiO (i. e. Ni^{+2}) to NiOOH (i.e. Ni^{+3}) which is the reversible redox process (eqn. 1) [35-36]. Further, the curve consists of a second peak at 0.37 V. This may be attributed due to the contribution of Ni foam (i.e. Ni^0) which can be converted into β-$Ni(OH)_2$ (i.e. Ni^{+2}) earlier at first redox peak 0.32 V (eqn. 2) followed by conversion from β-$Ni(OH)_2$ (i.e. Ni^{+2}) to NiOOH (i.e. Ni^{+3}) at 0.37 V (eqn. 3) [25, 37-38]. This process of double peaks at cathodic sweeps observed for the sample NiO@Ni (400°C) is likely due of the lower thickness of the oxide layer on the surface of Ni foam, or from regions devoid of NiO, that facilitates ion access to the Ni metal surface. Conversely, the process was not observed in the CV curve of the sample NiO@Ni(800°C), as the thickness of the oxide layer and its degree of Ni coverage increased during the recrystallization process. The process involved during these actions is as follows:

$$NiO + OH^- \leftrightarrow NiOOH + e^- \quad (1)$$

$$Ni^\circ + 2OH^- \rightarrow \beta Ni(OH)_2 + 2e^- \quad (2)$$

$$\beta Ni(OH)_2 + OH^- \rightarrow NiOOH + H_2 \quad (3)$$

The specific capacitance of the samples NiO@Ni (400°C) and NiO@Ni (800°C) derived from the CV curves is shown in Figure 5 (c). Specifically, the maximum specific capacitance calculated was found to be 184 F cm^{-2} and 265 F cm^{-2} at 5 mV s^{-1} scan rate for NiO@Ni (400°C) and NiO@Ni (800°C), respectively. The specific capacitance steadily reduces with faster potential scan rate (from 5 mV to 50 mV) for both materials as shown in Figure 5(c). Figure 5 (b) shows the GCD measurements carried out at

1 A g^{-1} for Ni, NiO@Ni(400°C) and NiO@Ni(800°C). The data endorse the non-linear behaviourr supporting the pseudocapacitive nature of the response [39]. To compare with the specific capacitance result from CV curves, the SC values were also calculated from GCD measurement curves. The obtained values for NiO@Ni(400°C) and NiO@Ni(800°C) were 108 F cm^{-2} and 164 F cm^{-2}, respectively. The specific capacitance values are decreasing with respect to the increasing current density as depicted from Figure 5 (d).

Figure 6(a) shows the CV curves obtained for Ni, NiO@Ni(N_2–800°C) and NiO@Ni(Ar–800°C) at scan rate of 10 mV s^{-1} within a potential window of 0-0.6 V *vs.* SCE. Akin to Ni samples annealed at 400 and 800°C, the peaks formed at the respective anodic and cathodic sweeps for NiO@Ni(N_2–800°C) and NiO@Ni(Ar–800°C) indicate the pseudocapacitive behavior of the Ni foams following annealing in N_2 or Ar. The CV curves of the samples NiO@Ni(N_2–800°C) and NiO@Ni(Ar–800°C) are composed of redox peaks in the cathodic sweep at 0.24 V and 0.23 V, respectively, corresponding to the conversion of surface NiO (i.e. Ni^{+2}) to NiOOH (i.e. Ni^{+3}) which is the reversible redox process (eqn.1)[35-36]. Further, the curves consist of a second peak at 0.26 V and 0.32 V for NiO@Ni(N_2–800°C) and NiO@Ni(Ar–800°C). This may be attributed due to the contribution of Ni foam (i.e. Ni^0) which can be converted into β-$Ni(OH)_2$ (i.e. Ni^{+2}) at the first redox peak at ~0.24V (eqn. 2) followed by conversion from β-$Ni(OH)_2$ (i.e. Ni^{+2}) to NiOOH (i.e. Ni^{+3}) at 0.26 V and 0.32 V, respectively, for Ni foam annealed in N_2 and Ar (eqn. 3). [25, 37-38] This process of double peaks at cathodic sweeps observed for the samples NiO@Ni(N_2–800°C) and NiO@Ni(Ar–800°C) is due to the $Ni(OH)_2$ and NiOOH formation on Ni in strong base, following NiO formation upon exposure to air after inert environment annealing. The specific capacitance of the samples NiO@Ni(N_2–800°C) and NiO@Ni(Ar–800°C) derived from the CV curves is shown in Figure 6(c). The maximum specific capacitance calculated was found to be 256.8 F cm^{-2} and 291.2 F cm^{-2} at 10 mV s^{-1} scan rate for the samples NiO@Ni(N_2–800°C) and NiO@Ni(Ar–800°C), respectively. The specific capacitance also reduces with increased potential scan rate (from 5 mV to 50 mV) for both the samples as shown in Figure 6(c), similar to the behaviour of samples annealed in air at both temperatures, confirming a similar involvement of NiO and related oxidized phases of Ni. Figure 6 (b) shows the GCD measurements curves carried at 1 A g^{-1} for Ni, NiO@Ni(N_2–800°C) and NiO@Ni(Ar–800°C), and also confirms a pseudocapacitive behaviour from an oxidized Ni surface [39] following annealing in inert environment and subsequent air exposure. To compare with the specific capacitance result from CV curves, the SC values were calculated from GCD measurement curves. The obtained values for samples NiO@Ni(N_2–800°C) and NiO@Ni(Ar–800°C) were 164 F cm^{-2} and 182 F cm^{-2}, respectively. The specific capacitance values are decreasing with respect to the increasing current density as depicted in Figure 6(d).

The variations in the SC values observed for all samples annealed in air at different temperatures as well as in different atmospheres of N_2 and Ar calculated from CV of course differ slightly from those obtained at constant current in GCD measurement curves. SC values are calculated from CV curves at the particular potential, while those calculated from GCD measurements curves are the time-integrated capacitance over the potential range 0–0.5 V [40-41]. Figure 5(e-f) and Figure 6(e-f) illustrate the reliance of voltammetric charge (q^*) on the scan rate of CV and compares the effect of the ion diffusion resistance of the oxide layer grown on the Ni surface during the annealing in air at 400°C and 800°C, and during the annealing in N_2 and Ar at 800°C, respectively. The voltammetric charge is usually recognized as a key parameter in assessing the electrochemically active sites between the sample surface oxide (i.e. NiO) and aqueous electrolyte. The outer charge (q_o^*) belonging to the region in contact with the electrolyte directly is used to estimate the active outer electrochemical surface, whereas the inner charge (q_i^*) indicates the region of pore, grain boundaries, voids and cracks etc. from the sample bulk and is used to estimate the active inner electrochemical surface. The total charge (q_t^*) is obtained from the intersection of q^* to $\nu = 0$ in the plot of $1/q^*$ versus $\nu^{1/2}$ as shown in Figure 5(e) and Figure 6(e). The quantity of outer charge (q_o^*) is obtained from the intersection of q^* to $\nu = \infty$ in the plot of q^* versus $1/\nu^{1/2}$ as shown in Figure 5(f) and Figure 6(f). From this information one can obtain the contribution due to the inner active surface by subtracting q_o^* from q_t^* [42-45]. The estimated values of the voltammetric charges and their ratios for samples annealed at 400℃ and 800℃ and those annealed in different environments are tabulated in Table 1. The ratios q_i^*/q_t^* and q_o^*/q_t^* for the NiO@Ni(400℃) are 0.39 and 0.60, whereas, those for NiO@Ni(800°C) is 0.23 and 0.77 respectively. However, the ratio q_i^*/q_t^* and q_o^*/q_t^* for the sample NiO@Ni(N_2-800°C) are 0.14 and 0.86, and those for NiO@Ni(Ar-800°C) are 0.25 and 0.75, respectively. Here, the results indicate a preferential outer charge contribution from the Ni oxide-electrolyte interface.

The EIS measurements confined within a frequency range of 0.1 to 10^5 Hz with a potential amplitude of 5 mV vs. SCE were carried out in 6 mol dm^{-3} KOH solution to compare the charge transport kinetics of the samples. Figure 7(a, b) shows the Nyquist plot and extended view in the high frequency region respectively, for NiO@Ni(400°C) and NiO@Ni(800°C). The inset shows the Nyquist plot of the Ni. Figure 7(c, d) shows the Nyquist plot and extended view in high frequency region respectively, for NiO@Ni(N_2-800°C) and NiO@Ni(Ar-800°C). The equivalent series resistance of a supercapacitor comprises ionic and electronic contributions. The electronic resistance is related to the intrinsic electronic resistance of the surface NiO particles layer and the interfacial resistances of particle-to-particle and particle-to current collector. The ionic resistance is linked with the electrolyte resistance in the pores and the ionic (diffusion) resistance of ions moving in small pores.[46-47] The equivalent series resistance (ESR) of samples was obtained from the intercept of real impedance at high frequency side. The ESR

values of Ni, NiO@Ni(400°C) and NiO@Ni(800°C) samples were 843.36 Ω, 0.35 Ω and 0.15 Ω, respectively and that for the samples NiO@Ni(N_2-800°C) and NiO@Ni(Ar-800°C) 0.28 Ω and 0.26 Ω respectively. These results clearly indicates that the relatively high impedance of untreated Ni foam (i.e. Ni) is significantly reduced to a very low impedance value after annealing in air atmosphere at 400°C and 800°C, and in N_2 and Ar at 800°C, which is similar to a classic metal annealing condition. The electrical conductivity improvement is due to grain boundary density reduction as expected from annealing of granular polycrystalline Ni in both environments. As such, annealing treatments do markedly improve the electrical conductivity of the foam as a current collector. However, the surface formation of oxyhdroxide and oxide phases in strong base, typical of supercapacitor electrolytes, does noticeably affect the nature of the charge storage process with the outer surface.

4. CONCLUSION

This investigation has demonstrated that annealing of Ni foam in air and in inert gases such as N_2 and Ar, can result in surface oxidation processes that alter the nature of charge storage processes with the Ni foam current collector when used in symmetric or asymmetric supercapacitors in aqueous electrolytes. After annealing at 400 and 800 °C in either air, N_2 or Ar at 800°C, we observe the formation of NiO@Ni confirmed by Raman scattering and electron microscopy. The recrystallization process, where metallic Ni^+ cations are activated to quickly form NiO with air during annealing in air forms the NiO layer on the surface of Ni foam, with an associated reduction in grain boundary resistance through the metallic Ni foam determined by EIS measurements. Whereas, during the annealing in the N_2 and argon environment the recrystallization process was initiated by replacement of loosely bound N^- and Ar^- by O^{2-} when exposed to air after annealing. The FESEM plan view images clearly show the NiO morphology and coverage in each case, where that NiO growth expands latterly over the sample surface initially. As the temperature reaches 400 or 800°C, the recrystallization process through diffusion of Ni^+ ions within the initially grown oxide layer allows continual oxide growth an thickening and conversion into NiO@Ni. The XPS analysis confirms the formation Ni-O bonding. The electrochemical measurements indicate pseudocapacitive behavior with the redox peaks at the respective anodic and cathodic sweeps characteristics of an oxidized Ni surface rather than a metallic one. As such, the changes to the Ni metal surface that can be caused by chemical environments, heating and high temperatures that typically occur when other active materials are grown on Ni directly, should be considered in the overall response of the electrode. This is especially true of the electrolyte can access to NiO surface, which in base undergoes transitions to $Ni(OH)_2$ and NiOOH phases from redox process that contribute to measured charge in voltammetric and galvanostatic measurements. Analysis of electrochemical data confirmed that the

majority (60 – 86%) of the stored charge from these annealed Ni foams arises from the processes at the non-metallic surface-electrolyte interface.

ACKNOWLEDGEMENTS

This work was supported by an Irish Research Council Government of Ireland Postdoctoral fellowship award under contract GOIPD/2016/575.

REFERENCES

[1] Goodenough, J. B. Evolution of strategies for modern rechargeable batteries, Acc. Chem. Res., 2013, 46, 1053–1061.

[2] Cheng, F. Y.; Liang, J.; Tao, Z. L.; Chen, J. Functional materials for rechargeable batteries, Adv. Mater. ,2011, 23, 1695–1715.

[3] Simon, P.; Gogotsi, Y. Materials for electrochemical capacitors, Nat. Mater.,2008, 7, 845-854.

[4] Sun, W.; Zheng, R.; Chen, X. Symmetric redox supercapacitor based on micro-fabrication with three-dimensional polypyrrole electrodes, Journal of Power Sources, 2010, 195, 7120–7125.

[5] Wang, C.; Zhan, Y.; Wu, L.; Li, Y.; Liu, J. High-voltage and high-rate symmetric supercapacitor based on MnO2-polypyrrole hybrid nanofilm, Nanotechnol. 2014, 25, 305401.

[6] Chen, P. C.; Shen, G.; Shi, Y.; Chen, H.; Zhou, C. Preparation and characterization of flexible asymmetric supercapacitors based on transition-metal-oxide nanowire/single-walled carbon nanotube hybrid thin-film electrodes, ACS Nano, 2010, 4, 4403–4411

[7] Sumboja, A.; Foo, C. Y.; Wang, X.; Lee, P. S., Large areal mass, flexible and free- standing reduced graphene oxide/manganese dioxide paper for asymmetric supercapacitor device, Adv. Mat., 2013, 25, 2809–2815.

[8] Feng, J. X.; Ye, S. H.; Lu, X. F.; Tong, Y. X.; Li, G. R. Asymmetric Paper Supercapacitor Based on Amorphous Porous Mn3O4 Negative Electrode and Ni(OH)2 Positive Electrode: A Novel and High-Performance Flexible Electrochemical Energy Storage Device, ACS Appl. Mat. Interfaces, 2015, 7, 11444–11451.

[9] Salunkhe, R. R.; Kamachi Y.; Torad, N. L.; Hwang, S. M.; Sun, Z.; Dou, S. X.; Kim J. H.; Yamauchi, Y. Fabrication of symmetric supercapacitors based on MOF-derived nanoporous carbons, J. Mater. Chem. A, 2014, 2,19848-19854.

[10] Eustache, E.; Frappier, R. R.; Porto, L.; Bouhtiyya, S.; Pierson J. F.; Brousse, T. Asymmetric electrochemical capacitor microdevice designed with vanadium nitride and nickel oxide thin film electrodes, Electrochemistry Communications, 2013, 28, 104–106.

[11] Syahidah, S. N.; Majid, S. R. Ionic liquid-based polymer gel electrolytes for symmetrical solid-state electrical double layer capacitor operated at different operating voltages, Electrochimica Acta, 2015, 175, 184–192.

[12] Vadiyar, M. M.; Bhise, S. C.; Ghule, K.; Kolekar, S. S.; Chang J.; Ghule, A. V. Low cost flexible 3-D aligned and cross-linked efficient ZnFe2O4 nano-flakes electrode on stainless steel mesh for asymmetric supercapacitors, J. Mater. Chem. A, 2016, 4, 3504-3512.

[13] Huang, L.; Chen, D.; Ding, Y.; Feng, S.; Wang, Z. L.; Liu, M. L. Nickel–cobalt hydroxide nanosheets coated on $NiCo_2O_4$ nanowires grown on carbon fiber paper for high-performance pseudocapacitors, Nano Lett. 2013, 13, 3135−3139

[14] Lin J. H.; Jia H. N.; Cai Y. F.; Chen S. L.; Liang H.; Wang X;, Zhang F.; Qi J. L.; Cao J.; Feng J. C. and Fei W. D.; Modifying the electrochemical performance of vertically-oriented few-layered graphene through rotary plasma processing, J. Mater. Chem. A, 2017, 6, 908-917.

[15] Jia H.; Wang Z.; Zheng X.; Lin J.; Liang H.; Cai Y.; Qi J.; Cao J.; Feng J.; Fei W.; Interlaced Ni-Co LDH nanosheets wrapped Co9S8 nanotube with hierarchical structure toward high performance supercapacitors, Chemical Engineering Journal, 2018, 351, 348-355.

[16] Ma F. X.; Yu L.; Xub C. Y. Lou X. W.; Self-supported formation of hierarchical NiCo2O4 tetragonal microtubes with enhanced electrochemical properties, Energy Environ. Sci., 2016, 9, 862-866.

[17] Wu, S.; Hui, K. S.; Hui K. N.; Kim, K. H. Ultrathin porous NiO nanoflake arrays on nickel foam as an advanced electrode for high performance asymmetric supercapacitors, J. Mater. Chem. A, 2016, 4, 9113-9123.

[18] Cai, D.; Huang, H.; Wang, D.; Liu, B.; Wang, L.; Liu, Y.; Li, Q.; Wang, T. High-Performance Supercapacitor Electrode Based on the Unique ZnO@Co_3O_4 Core/Shell Heterostructures on Nickel Foam, ACS Appl. Mater. Interfaces, 2014, 6, 15905–15912.

[19] Jiang, J.; Li, Y.; Liu, J.; Huang, X.; Yuan C.; Lou X. W. Recent advances in metal oxide- based electrode architecture design for electrochemical energy storageAdv. Mater. 2012, 24, 5166−5180.

[20] Reddy, A. L. M.; Gowda, S. R.; Shaijumon, M. M.; Ajayan, P. M., Hybrid nanostructures for energy storage applications, Adv. Mater.2012, 24, 5045−5064.

[21] Zhang, G.; Wang, T.; Yu, X.; Zhang, H.; Duan H.; Lu, B. Nanoforest of hierarchical Co3O4@NiCo2O4 nanowire arrays for high-performance supercapacitors, Nano Energy 2013, 2, 586−594.

[22] Cheng, C.; Fan, H. J. Branched nanowires: Synthesis and energy applications, Nano Today 2012, 7, 327−343.

[23] Xiong, Q.; Tu, J.; Xia, X.; Zhao, X. Y.; Gu, C. D.; Wang, X. L. A three-dimensional hierarchical Fe2O3@NiO core/shell nanorod array on carbon cloth: a new class of anode for high-performance lithium-ion batteries, Nanoscale, 2013, 5, 7906−7912.

[24] Wu, C.; Cai, J.; Zhang, Q.; Zhou, X.; Zhu, Y.; Shen, P. K.; Zhang, K. Hierarchical Mesoporous Zinc−Nickel−Cobalt Ternary Oxide Nanowire Arrays on Nickel Foam as High-Performance Electrodes for Supercapacitors, ACS Appl. Mater. Interfaces 2015, 7, 26512−26521

[25] Drunen, J. V.; Kinkead, B.; Wang, M. C. P.; Sourty, E.; Gates, B. D; Jerkiewicz, G. Comprehensive Structural, Surface-Chemical and Electrochemical Characterization of Nickel-Based Metallic Foams, ACS Appl. Mater. Interfaces 2013, 5, 6712−6722.

[26] Kumari, S. V.; Natarajan, M.; Vaidyan, V. K.; Koshy, P. Surface oxidation of nickel thin films J. Mater. Sci. Lett. 1992, 11, 761

[27] Cabrera N.; Mott, N. F., Theory of the oxidation of metals, Rep. Prog. Phys.,1949, 12, 163.

[28] Valladares, L. D. L. S.; Ionescu, A.; Holmes, S.; Barnes, C. H. W.; Dominguez, A. B.; Quispe, O. A.; Gonzalez, J. C.; Milana, S.; Barbone, M.; Ferrari, A. C.; Ramos, H.; Majima, Y. Characterization of Ni thin films following thermal oxidation in air, J. Vac. Sci. Technol. B, 2014, 32(5), , 051808-1-051808-8

[29] Ferrari A. C.; Robertson, J. Interpretation of Raman spectra of disordered and amorphous carbon, Phys Rev B, 2000, 61, 14095-14107.

[30] Lin J.; Liu Y.; Wang Y.; Jia H.; Chen S.; Qi J.; Qu C.; Cao J.; Fei W.; Feng J.; Rational construction of nickel cobalt sulfide nanoflakes on CoO nanosheets with the help of carbon layer as the battery-like electrode for supercapacitors, Journal of Power Sources, 362 (2017) 64-72.

[31] Varghese, B.; Reddy, M. V.; Yanwu, Z.; Lit, C. S.; Hoong, T. C.; Rao, G. V. S.; Chowdari, B. V. R.; Wee, A. T. S.; Lim C. T.; Sow, C. H. Fabrication of NiO Nanowall Electrodes for High Performance Lithium Ion Battery, Chem. Mater. 2008, 20, 3360−3367.

[32] Liang, K.; Tang X.; Hu, W. High-performance three-dimensional nanoporous NiO film as a supercapacitor electrode, J.Mater. Chem. 2012, 22, 11062−11067.

[33] Holloway, P. H.; Hudson, J. B. Kinetics of the reaction of oxygen with clean nickel single crystal surfaces: I. Ni(100) surface, Surf. Sci. 1974, 43, 123–140.

[34] Yan, J.; Fan, Z.; Sun, W.; Ning, G.; Wei, T.; Zhang, Q.; Zhang, R.; Zhi, L.; Wei, F. Advanced Asymmetric Supercapacitors Based on Ni(OH)2/Graphene and Porous Graphene Electrodes with High Energy Density, Adv. Funct. Mater. 2012, 22, 2632-2641

[35] Kore, R. M.; Mane, R. S.; Naushad, M.; Khanand, M. R.; Lokhande, B. J. Nanomorphology-dependent pseudocapacitive properties of NiO electrodes engineered through a controlled potentiodynamic electrodeposition process, RSC Adv., 2016, 6, 24478-24483.

[36] Meher, S. K.; Justin, P.; Rao, G. R. Nanoscale morphology dependent pseudocapacitance of NiO: Influence of intercalating anions during synthesis, Nanoscale, 2011, 3, 683-692.

[37] Alsabet, M.; Grden, M.; Jerkiewicz, G. Electrochemical Growth of Surface Oxides on Nickel. Part 1: Formation of α-Ni(OH)2 in Relation to the Polarization Potential, Polarization Time, and Temperature, Electrocatalysis, 2011, 2,317−330.

[38] Jouanneau, A.; Keddan, M.; Petit, M. C. A general model of the anodic behaviour of nickel in acidic media, Electrochim. Acta 1976,21, 287−292.

[39] Sugimoto, W.; Iwata, H.; Yasunaga, Y.; Murakami, Y.; Takasu, Y. Preparation of Ruthenic Acid Nanosheets and Utilization of Its Interlayer Surface for Electrochemical Energy Storage, Angew. Chem., Int. Ed., 2003, 42, 4092-4096.

[40] Kelly, T. L.; Yano, K.; Wolf, M. O. Supercapacitive Properties of PEDOT and Carbon Colloidal Microspheres, ACS Appl. Mater.Interfaces, 2009, 1, 2536-2543.

[41] Saravanakumar, B.; Purushothaman K. K.; Muralidharan, G. Interconnected V_2O_5 Nanoporous Network for High-Performance Supercapacitors, ACS Appl. Mater. Interfaces, 2012, 4, 4484-4490.

[42] Baronetto, D.; Krstajic, N.; Trasatti, S. Reply to "note on a method to interrelate inner and outer electrode areas" by H. Vogt, Electrochim. Acta 1994, 39, 2359-2362.

[43] Soudan, P.; Gaudet, J.; Guay, D.; Belanger, D.; Schulz, R. Electrochemical Properties of Ruthenium-Based Nanocrystalline Materials as Electrodes for Supercapacitors, Chem. Mater. 2002, 14, 1210-1215.

[44] Chang, J.; Park, M.; Ham, D.; Ogale, S. B.; Mane, R. S.; Han, S. H.; Liquid-phase synthesized mesoporous electrochemical supercapacitors of nickel hydroxide, Electrochim.Acta 2008,53, 5016-5021.

[45] Shaikh, S. F.; Lim, J. Y.; Mane, R. S.; Han, S. H.; Ambade, S. B.; Joo, O.S. Wet-chemical polyaniline nanorice mass-production for electrochemical supercapacitors, Synth. Met. 2012, 162, 1303-1307.

[46] Wen, Z. B.; Qu, Q. T.; Gao, Q.; Zheng, X. W.; Hu, Z. H.; Wu, Y. P.; Liu Y. F.; Wang, X. J. An activated carbon with high capacitance from carbonization of a resorcinol–formaldehyde resin, Electrochem. Commun., 2009, 11, 715-718.

[47] Pandolfo A. G.; Hollenkamp, A. F. Carbon properties and their role in supercapacitors, J. Power Sources, 2006,157, 11-27.

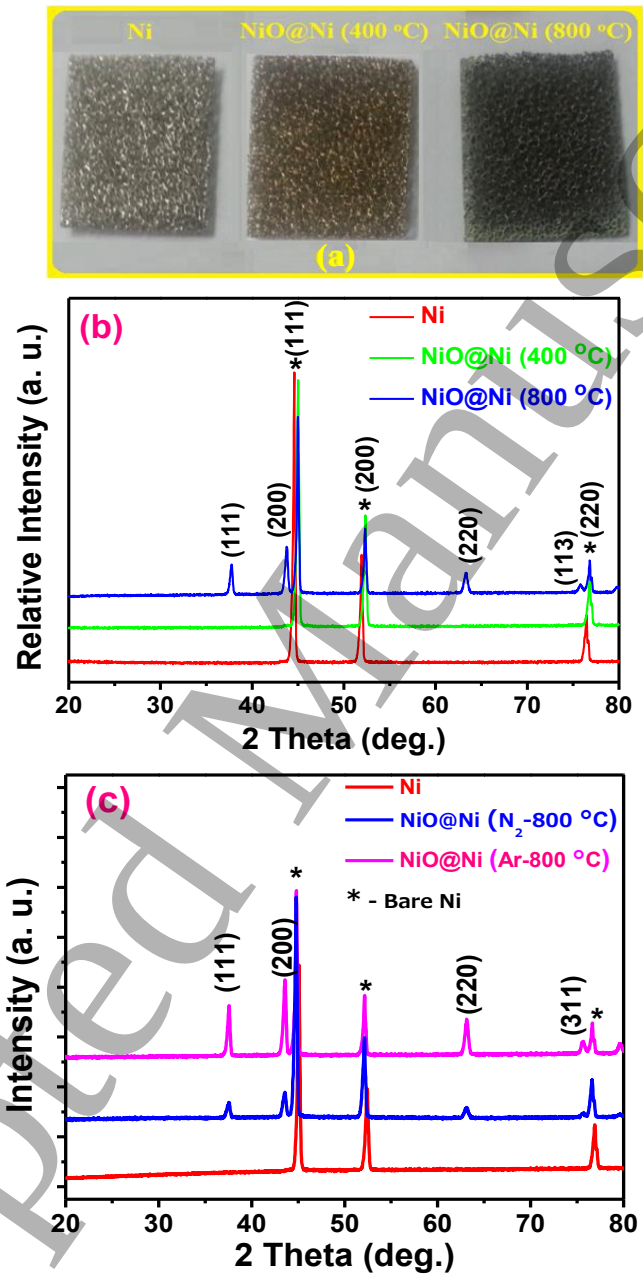

Figure 1: (a) Digital photoimages of Ni, NiO@Ni(400°C), and NiO@Ni(800°C) samples. (b) XRD patterns of Ni, NiO@Ni(400°C), and NiO@Ni(800°C). (c) XRD patterns of Ni, NiO@Ni (N_2-800°C) and NiO@Ni(Ar-800°C) obtained from annealing of Ni foam in N_2 and Ar atmospheres.

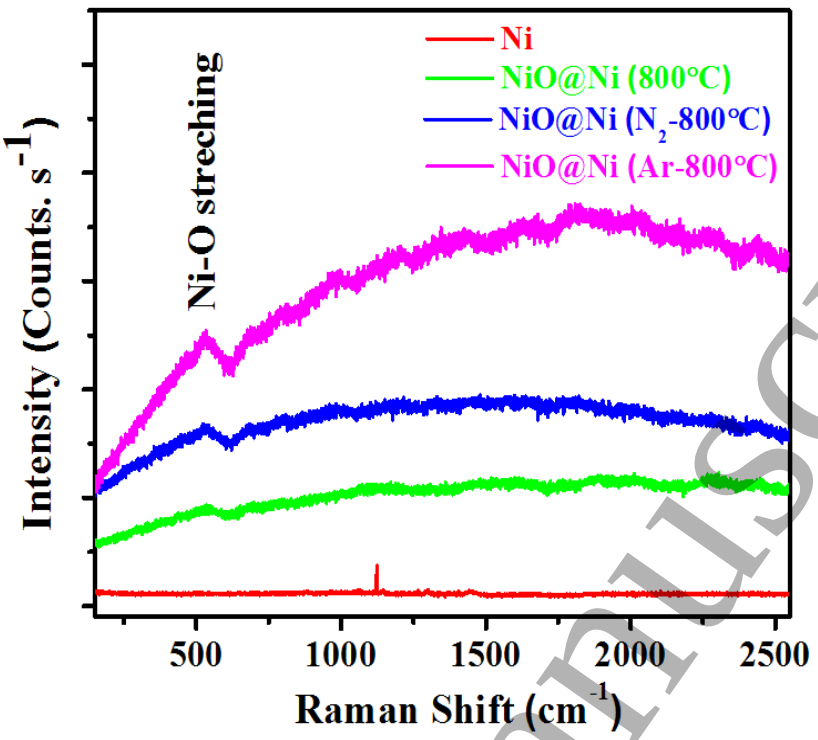

Figure 2: Raman spectra of Ni, NiO@Ni (800°C), NiO@Ni (N_2-800°C) and NiO@Ni (Ar-800°C).

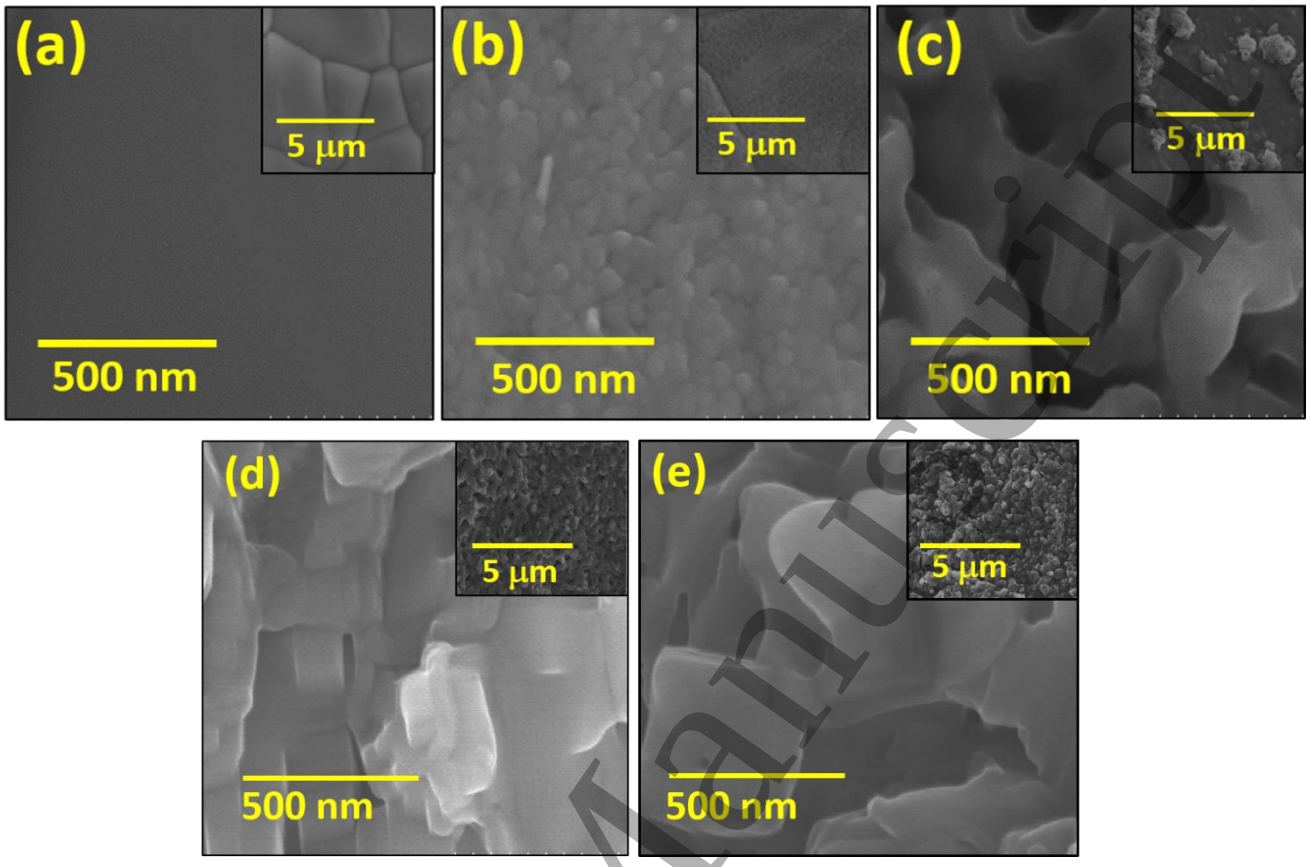

Figure 3: FE-SEM plan images of (a) Ni, (b) NiO@Ni(400°C), (c) NiO@Ni(800°C), (d) NiO@Ni(Ar - 800°C) and (e) NiO@Ni(N_2 - 800°C).

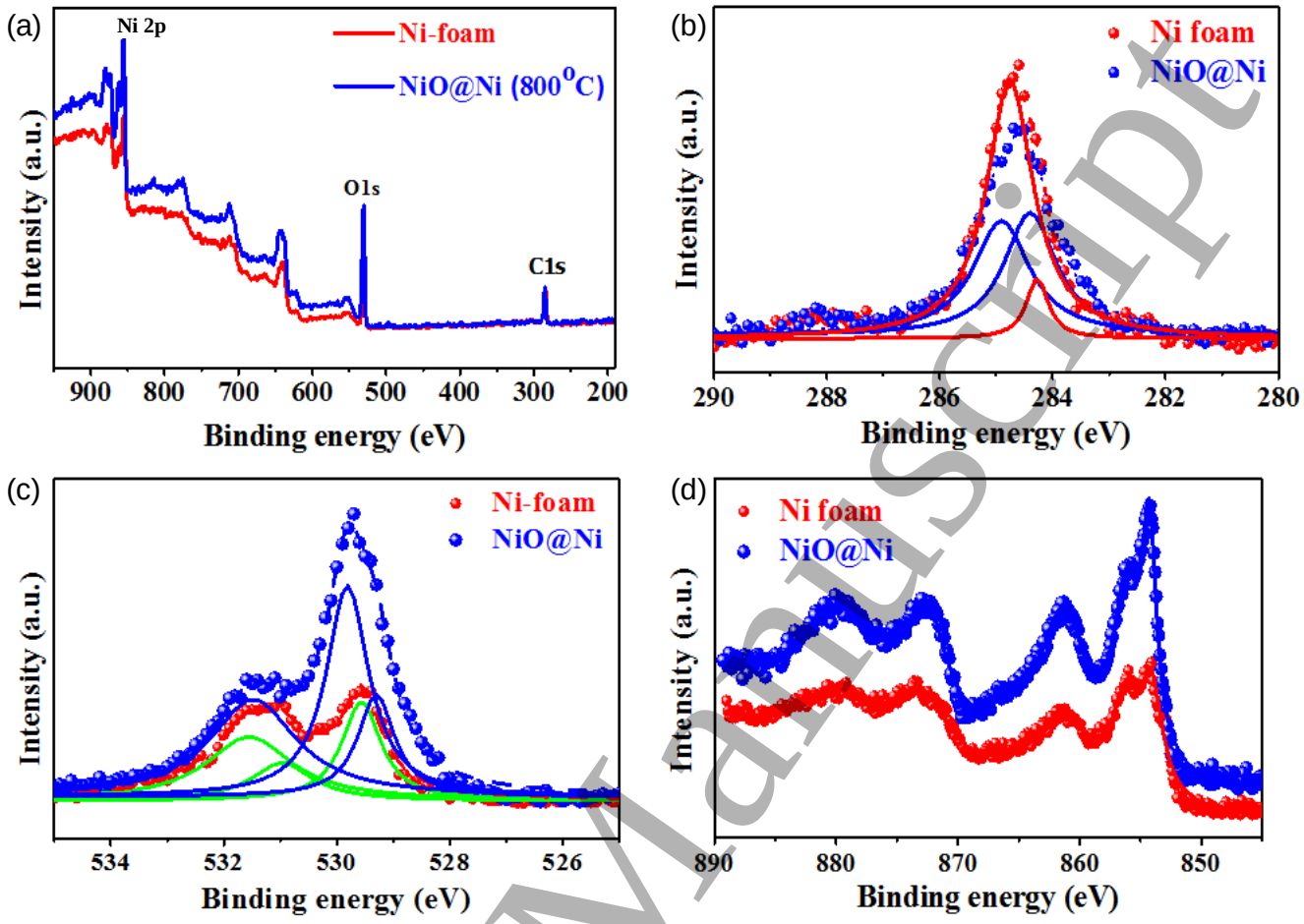

Figure 4: (a) XPS survey spectrum and (b) C 1s, (c) O 1s, (d) Ni 2p core-levels obtained from Ni foam and NiO@Ni(800°C).

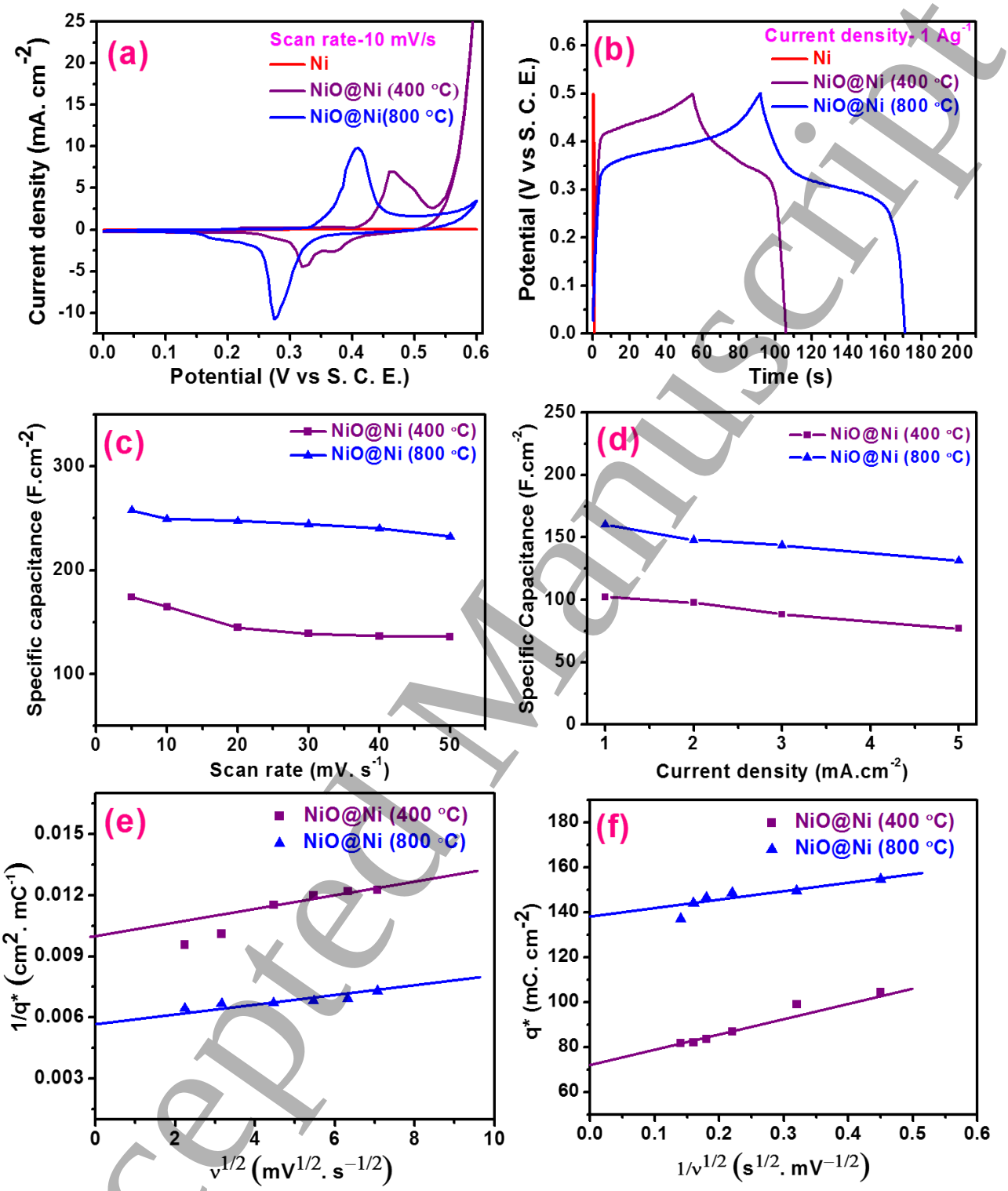

Figure 5. (a) CV curves at 10 mV/s scan rate, (b) GCD curves at 1A/g current density, (c) SC *vs.* scan rate variation, (d) SC *vs.* current density variation, and (e) plots of $1/q^*$ *vs.* $v^{1/2}$and (f) q^* *vs.* $1/v^{1/2}$ for NiO@Ni (400°C) and NiO@Ni(800°C).

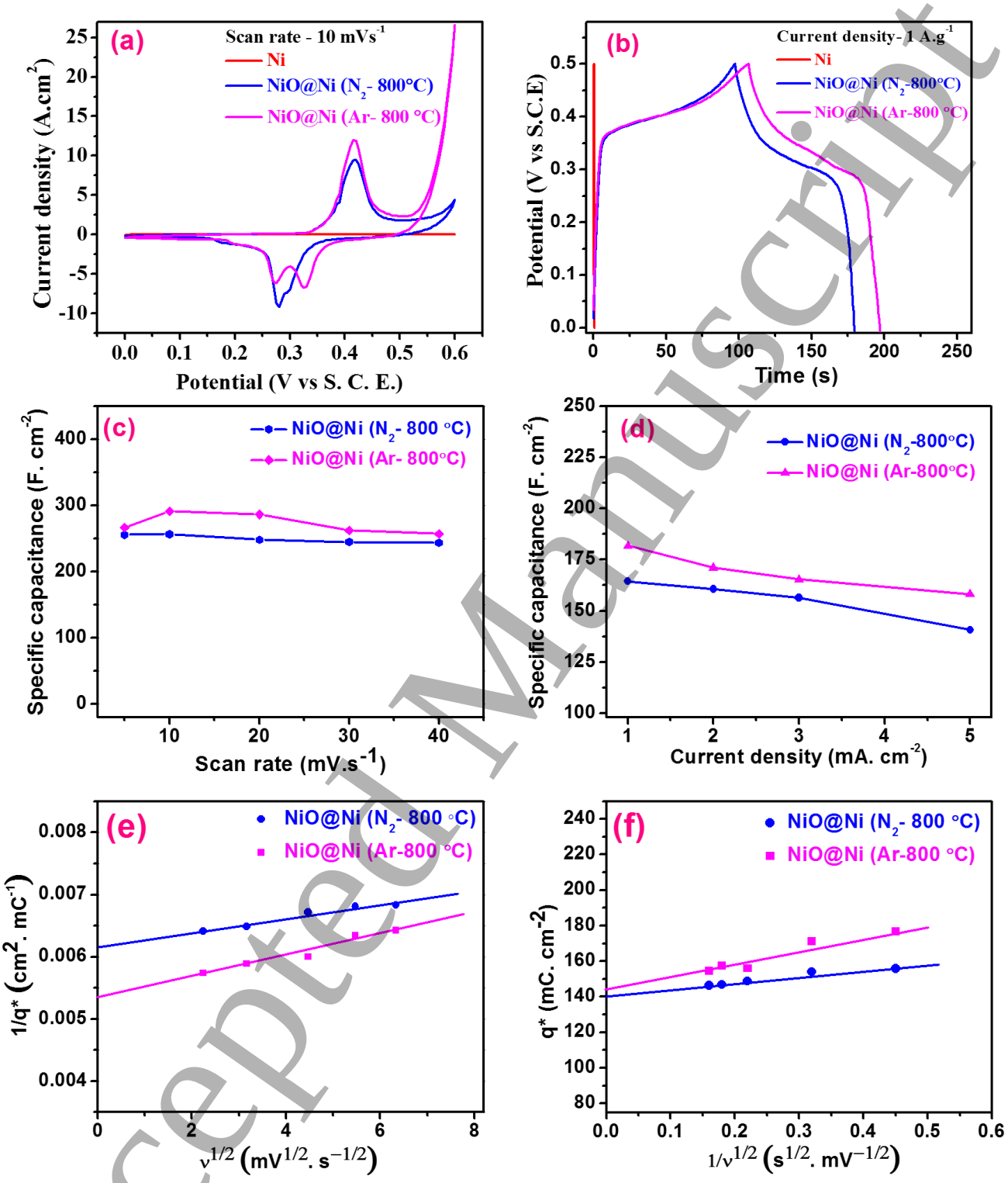

Figure 6. (a) CV curves at 10 mV/s scan rate, (b) GCD curves at 1 A/g current density, (c) SC *vs.* scan rate variation, (d) SC *vs.* current density variation, and (e) plots of 1/q* *vs.* $v^{1/2}$and (f) q* *vs.* $1/v^{1/2}$ for the samples NiO@Ni (N_2-800°C) and NiO@Ni(Ar-800°C).

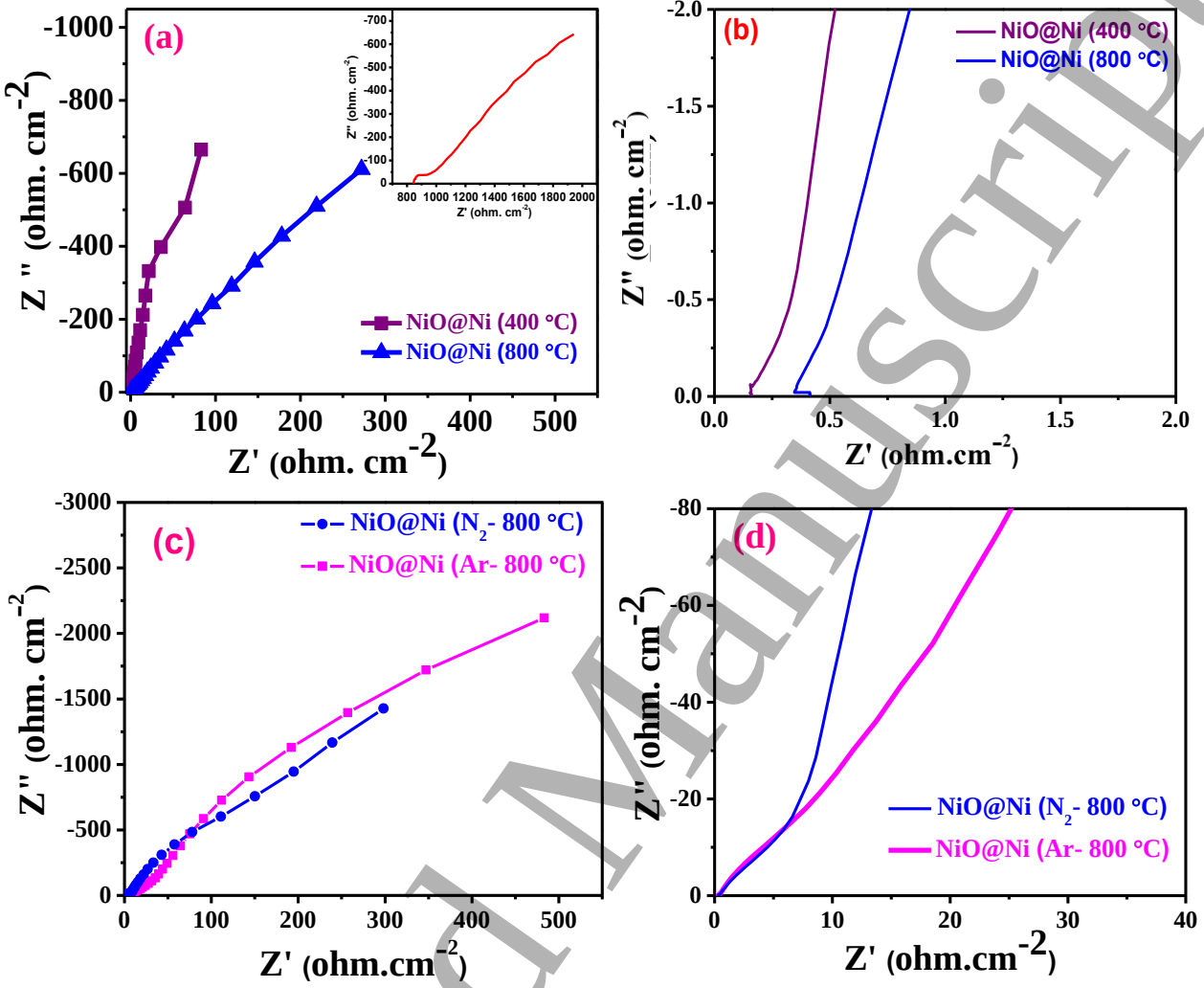

Figure 7: Nyquist plots of (a) NiO@Ni (400°C) and NiO@Ni(800°C). The inset shows the Nyquist plot of Ni foam. (b) The NiO@Ni (400°C) and NiO@Ni(800°C) EIS spectra in the high frequency region. (c) EIS Nyquist plots of NiO@Ni (N_2-800°C) and NiO@Ni (Ar-800°C) and (d) corresponding spectral response in high frequency region.

Table 1: Inner and outer surface charge contribution determined from analysis of CV acquired as a function of scan rate.

Electrode	q_t*(mC. cm^{-2})	q_o* (mC. cm^{-2})	q_i* (mC.cm^{-2})	q_i*/q_t*	q_o*/q_t*
NiO@Ni(400 °C)	99.01	72.76	26.25	0.39	0.60
NiO@Ni(800 °C)	178.06	137.35	40.71	0.23	0.77
NiO@Ni(N_2-800 °C)	163.93	140.65	23.28	0.14	0.86
NiO@Ni(Ar-800 °C)	192.32	144.14	49.38	0.25	0.75